



Polymeric graphitic carbon nitride nanosheet-coated amorphous carbon supports for enhanced fuel cell electrode performance and stability

In Hyuk Lee^{a,b,c}, Jinwon Cho^a, Keun Hwa Chae^d, Min Kyung Cho^d, Juhae Jung^b, Jongin Cho^b, Hyun Jin Lee^b, Hyung Chul Ham^a, Jin Young Kim^{a,c,*}

^a Fuel Cell Research Center, Korea Institute of Science and Technology, Hwarangno 14-gil 5, Seongbuk-gu, Seoul, 02792, Republic of Korea

^b Doosan Corporation Electro-Materials, 10, Suji-Ro(Si) 112 Beon-Gil, Suji-Gu, Yongin-Si, Gyeonggi-do, Republic of Korea

^c University of Science and Technology, Daejeon, 305-355, Republic of Korea

^d Advanced Analysis Center, Korea Institute of Science and Technology, Hwarangno 14-gil 5, Seongbuk-gu, Seoul, 02792, Republic of Korea

ARTICLE INFO

Keywords:

Catalyst support
Durability of PEMFC materials
Electrochemical carbon instability
Proton exchange membrane fuel cells (PEMFCs)
Surface modification

ABSTRACT

Carbon blacks, which consist of the assemblies of small graphene clusters having a spherical concentric packing structure, are amorphous and have widely been used as catalyst supports for proton exchange membrane fuel cell (PEMFC) electrodes. However, poor electrochemical corrosion resistance during extended use and repeated cyclic operation of PEMFCs shortens their practical device lifetime; surface defects, such as nanosized disordered domains, have been established as the most influential factors. Herein, we coupled polymeric graphitic carbon nitride (pg-CN) with amorphous carbon black (a-CB) in a core@shell structure to produce an electrochemically efficient and stable electrocatalyst support. Our protocol allowed for the simultaneous optimization of uniformly thin graphitic shell structures for electrochemical corrosion stability and nitrogen-enriched functionalities on the carbon surfaces for electrocatalyst (e.g., platinum) nucleation. The newly prepared a-CB@pg-CNs enhanced the stable fuel cell devices operation and remained invariant even at high potential (1.2–1.7 V). Significantly, when used for constructing the PEMFC electrode, a-CB@pg-CN support-based Pt catalyst electrodes outperformed and exhibited superior stability over state-of-the-art commercial a-CB-based counterparts. Experimental observations and density functional theory (DFT) calculations revealed that the unusual electrocatalytic properties of as-prepared a-CB@pg-CNs originated from an intrinsic chemical and electronic coupling that synergistically reduced electrochemical corrosion kinetics and promoted catalyst–support interactions.

1. Introduction

The oxygen reduction reaction (ORR) is a fundamental aspect of proton exchange membrane fuel cell (PEMFC) electrochemistry and is key to understanding the mechanism of other multi-electron transfer processes in electrocatalysis [1–3]. The ORR requires a favorable electrocatalyst electrode to achieve fast reaction kinetics for practical electrochemical applications [4,5]. Among the wide variety of available electrocatalysts, platinum (Pt) supported on carbon (Pt/C) displays superb electrocatalytic ORR performance including extremely high exchange current density and low onset potential [6].

Furthermore, to achieve a sustainable electrochemical ORR, the catalyst electrode should retain high electrocatalytic stability; however, this may present great challenges for electrodes under severe working conditions including high working electrode potential and a water-rich environment [7–12]. Especially under the frequently dynamic start-up and shut-down operations, the electrochemical carbon instability along

with the dissolution and/or loss of Pt surface area in the electrode have been identified as the most serious issues [13–15]. These issues are driving research to achieve the stability targets necessary for commercial PEMFC applications [16–19].

Currently, the most widely used support material is amorphous carbon black (a-CB) [14]. However, it suffers from an inherent electrochemical corrosion susceptibility to the acidic PEMFC electrochemical working condition [16,17]. Surface defects and catalyst–support interactions are the most influential factors [18]. The latter factor is of little importance if the carbonaceous matrix purely suffers from corrosion.

In this regard, there has been a move toward the development of more electrochemically stable supports [19–22]. However, despite tremendous efforts in identifying electrocatalyst supports that exhibit high stability to corrosion and that interact beneficially with the electrocatalyst particles, an efficient and practical electrocatalytic support system beyond amorphous carbon has not yet been found, essentially

* Corresponding author at: Fuel Cell Research Center, Korea Institute of Science and Technology, Hwarangno 14-gil 5, Seongbuk-gu, Seoul, 02792, Republic of Korea.
E-mail address: jinykim@kist.re.kr (J.Y. Kim).

narrowing the selection of competitive candidates to modified a-CB.

In this work, we report the preparation of thin, layered polymeric graphitic carbon nitride (pg-CN) nanosheet coatings onto a-CB. We demonstrate that the resulting core@shell-like a-CB@pg-CN hybrid possesses unique molecular structure and electronic properties for electrocatalytic ORR applications. This carbon hybrid contained polymeric graphitic shell structures with nitrogen-enriched surface moieties, and displayed comparable electrocatalytic ORR activity with current well-developed metallic Pt catalysts. Most importantly, it displayed excellent electrocatalytic stability compared with that of state-of-the-art commercial carbon supports in a real PEMFC device.

Electrochemical measurements in combination with density functional theory (DFT) calculations revealed that its unusual electrocatalytic properties originate from a synergistic effect of this hybrid nanostructure, in which the thin coating of pg-CN on a-CB facilitates the electrochemical ORR process with anticorrosive benefits at high potential regions (0.6–1.2 V). These research findings provide clear evidence that atomically surface-modified a-CB supports have great potential as highly efficient and stable electrocatalyst supports, thus opening a new avenue toward stabilizing a-CB for use in a wide variety of electrochemical applications.

2. Experimental

2.1. Synthesis of a-CB@pg-CN

Dicyandiamide (DCD) was dissolved in 50 ml of methanol solvent in round flask using sonication and then carbon black (Ketjen) was added to this solution. The solution was heated with stirring at 80 °C in an oil bath overnight. The resulting black powder was subsequently fired at 550 °C for 4 h with a heating rate of 10 °C/min in a quartz tube under Ar atmosphere, and we obtained black powder denoted a-CB@pg-CN.

2.2. Synthesis of Pt/a-CB@pg-CN

The a-CB@pg-CN (50 mg) was added directly to ethanol with ethanol. $\text{H}_2\text{PtCl}_6 \cdot 6\text{H}_2\text{O}$ (Sigma-Aldrich 33.2 mg) and oleylamine (100 μL) was added to the solution and then stirred for 12 h at room temperature. The reaction mixture was poured in solution of NaBH_4 (50 mg) with ethanol and then stirred for 12 h. Then the mixture was vacuum-filtered and then re-dispersed and washed in ethanol and deionized water, followed by a thermal treatment at 200 °C for 1 h in air condition and then for 2 h in Ar mixed 5% H_2 condition.

2.3. Material characterization

XPS spectra were measured with the K-ALPHA + surface analysis (Thermo scientific). TGA data was collected on a TA Instruments Q50, at a heating rate of 10 °C min^{-1} in nitrogen atmosphere. HRTEM micrographs were recorded using the TITAN TEM microscope. The Brunauer-Emmett-Teller (BET) surface area was measured by Micromeritics ASAP 2010 (V5.02) auto-adsorption analyzer with liquid N_2 adsorption at 77.40 K. The electrical conductivity were calculated from the following equation:

$$\rho = \frac{A \cdot R}{t}$$

$$\sigma = \frac{1}{\rho}$$

where ρ is electrical resistivity, R is electrical resistance, A is surface area of materials, L is length of materials and σ is electrical conductivity. The electrical resistance was measured by using a complex impedance analyzer (Bio-Logics, VMP3) at frequency of 1 kHz at room temperature using pellet-type sample.

2.4. Electrochemical half-cell test

The electrochemical measurements were carried out using a potentiostats Autolab PGSTAT20 and Metrohm Autolab connected in a three-electrode system at room temperature. The saturated calomel electrode (SCE) was calibrated against the reversible hydrogen electrode (RHE). Slurries have been prepared by mixing 5 mg carbon support materials, 50 mg Nafion resin (5 wt% Sigma-Aldrich) and 500 μL isopropyl alcohol with 30 min sonication and spread onto rotating disk electrode. CV were measured in an argon saturated 0.1 M HClO_4 electrolyte at a scan rate of 20 mV s^{-1} with 0 rpm from 0.05 to 1.05 V vs. RHE. The polarization curve obtained in oxygen saturated 0.1 M HClO_4 electrolyte at a scan rate of 5 mV s^{-1} with 1600 rpm from 0.05 to 1.05 V vs. RHE. The ADT was conducted in a potential range from 1.2 to 1.7 V vs. RHE in argon saturated 0.1 M HClO_4 electrolyte at a scan rate of 250 mV s^{-1} with 0 rpm for support materials and the ADT was conducted in a potential range from 0.6 to 1.2 V versus RHE in oxygen saturated 0.1 M HClO_4 electrolyte at a scan rate of 250 mV s^{-1} with 0 rpm for Pt loaded catalyst.

The ECSA for the Pt catalyst was calculated from the following equation [23].

$$\text{ECSA} = Q / (m \times \beta)$$

where Q is the charge for hydrogen desorption calculated from CV, m is the quantity of Pt on electrode and β is 210 $\mu\text{C cm}^{-2}$ represents the charge required to oxidize a monolayer of H_2 on smooth Pt.

2.5. MEA test

The catalyst slurry for the half-cell test was used for MEA preparation, which was sprayed to deposit it on Nafion 211 membrane. Pt loadings of 0.1 $\text{mg}_{\text{Pt}}/\text{cm}^2$ and 0.4 $\text{mg}_{\text{Pt}}/\text{cm}^2$ under 5 cm^2 were used for anode and cathode, respectively. MEA was placed between gas diffusion layers (SGL-39BC) and a gasket surrounding periphery of the laminate.

2.6. DFT calculation

The calculations were performed on the basis of spin polarized density functional theory (DFT) within the generalized gradient approximation (GGA) and the model of Perdew, Burke, and Ernzerhof (PBE), as implemented in the Vienna Ab Initio Simulation Package (VASP) [24,25]. The projector augmented wave (PAW) method with a plane wave basis set was employed to describe the interaction between the core and valence electrons [26]. Details are described in the supplementary information.

3. Results and discussion

3.1. Structure analysis of a-CB@pg-CN

Fig. 1a illustrates the preparation of a-CB@pg-CN by a relatively simple process. The preparation of these carbon composite materials involved impregnation of dissolved dicyandiamide (DCDA) into the a-CB surface and then using polycondensation to form more condensed polymeric network structures such as melamine, melem, and melon units. Polymeric carbon nitride sheet-like units formed graphitic structures directly on the surface of a-CB particles (Fig. 1a). The functionality of the support could be tailored as the ratio of primary to tertiary amine changed during this reaction. Finally, the intermediate products were dried and annealed at 550 °C for 4 h under an argon atmosphere to provide the final core@shell-like a-CB@pg-CN.

Scanning transmission electron microscopy (STEM) combined with electron energy-loss spectroscopy (EELS) was used to study the a-CB@pg-CN directly to prove the unique core@shell nanostructure (Fig. 1b). Spatial information concerning the a-CB@pg-CN sample was obtained

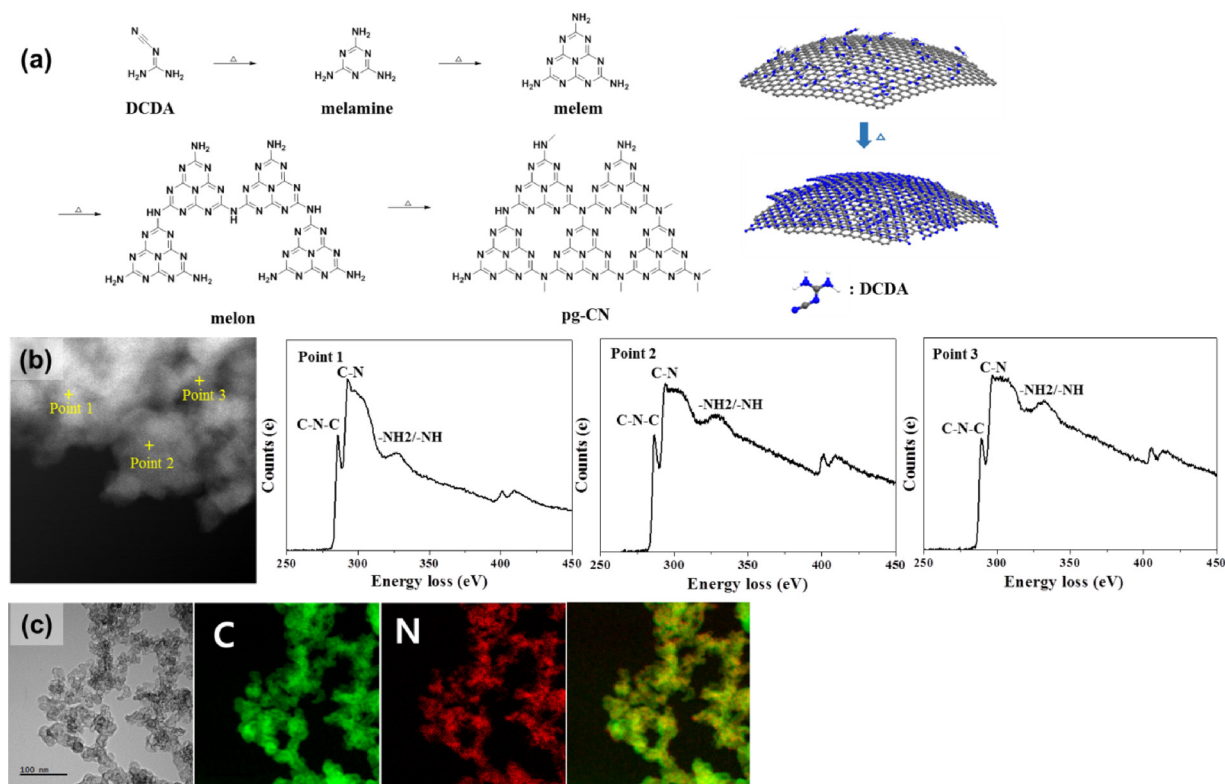


Fig. 1. (a) Schematic illustration of the synthesis procedure to obtain a-CB@pg-CN, (b) STEM image combined with EELS data obtained from three different regions of an a-CB@pg-CN, (c) energy-dispersive X-ray mapping of a-CB@pg-CN.

by examining the intensity variation of the energy-loss peaks. Fig. 1b shows STEM-EELS spectra that were collected from several regions of an a-CB@pg-CN sample (points 1–3 in Fig. 1b). The carbon K-edge EELS showed one energy-loss peak that was assigned to C–N–C species and the nitrogen K-edge showed three peaks corresponding to C–N–C, C–N, and –NH₂/–NH in order of low to high energy loss. The EELS mapping with these energy-loss peaks is typical of pure pg-CN and revealed that pg-CN was present over the entire region. This indicated that pg-CN was successfully coated on each a-CB subunit of the nanostructure.

Furthermore, energy-dispersive X-ray mapping of a-CB@pg-CN (Fig. 1c) demonstrated that the C (green) and N (red) were uniformly distributed over the a-CB@pg-CN nanoparticles. This also indicated homogeneous coating, in accordance with STEM-EELS observations. In principle, the pg-CN could be located on the outer surface or inside the pores of the a-CB. In an earlier work employing a similar technique, removal of the inner structures clearly revealed that pg-CN formed inside the hierarchical pores [27]. In this work, a decrease in pore size was observed when a-CB was impregnated with pg-CN, which suggested thin homogeneous coating on the inner pore walls.

3.2. Electrochemical stability of a-CB@pg-CN

3.2.1. Band structure analysis

Our development of a-CB@pg-CN electrocatalyst supports was motivated by the desire to impart better stability against corrosion while maintaining efficient transport within the electrodes during electrochemical processes. Insight into the improved electrochemical resistance of pg-CN materials against corrosion compared to a-CB were obtained from simple band-structure considerations. The allowed energy states of conductive carbons span across the H⁺/H₂ and O₂/H₂O potentials, which may originate from the non-crystalline structures (e.g., Urbach tails), and thus provide competitive electrochemical reduction and oxidation sites accessible under PEMFC conditions.

In contrast to a-CB, pg-CN has a crystalline structure, and the carbon atoms in pg-CN are bonded to nitrogen atoms having fully satisfied valence states and are thus fully oxidized. This chemistry opens a clean bandgap that brackets the H⁺/H₂ and O₂/H₂O potentials and therefore electrochemical corrosion of the C–N backbone is thermodynamically unfavorable under electrochemical PEMFC device operation (Fig. 2a) [14]. It has been reported that electrochemical oxidation of carbon is

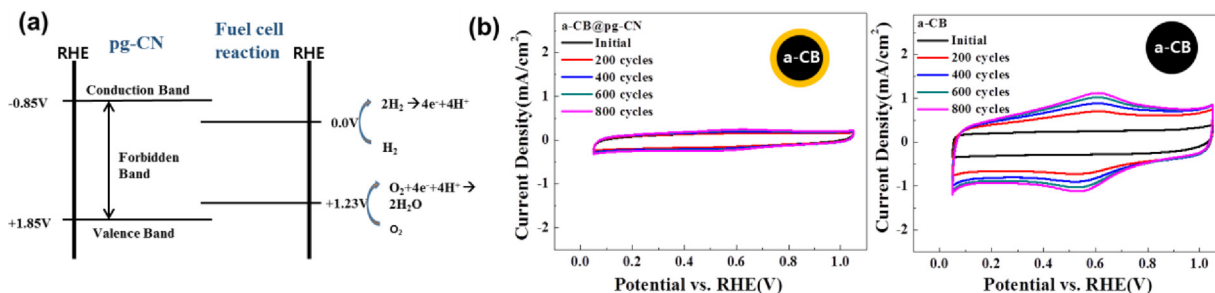


Fig. 2. (a) Energy level of electronic states of pg-CN and H⁺/H₂ and O₂/H₂O potentials, (b) cyclic voltammetry (CV) curves of a-CB (left) and a-CB@pg-CN (right) at a scan rate of 50 mV s^{−1} in an argon-saturated 0.1 M HClO₄ solution after accelerated durability testing (ADT) at 1.2–1.7 V.

thermodynamically allowable at a potential of 0.207 V, but such oxidation is believed to be slow [28]. The reactions rapidly increase at potentials above 0.9 V vs. RHE. However, most PEMFC electrode processes occur at potentials that do not necessarily correspond to the theoretical thermodynamic potentials to operate a PEMFC and that diverse kinetic parameters such as activation overpotentials may play a significant role in real PEMFC device processes.

3.2.2. Accelerated degradation tests (ADTs)

To examine the impact of the pg-CN coating on a-CB on the electrochemical carbon oxidation rate, we carried out cyclic voltammetry (CV) scans of a-CB@pg-CN samples cycling under the high potential regime ranging from 1.2 to 1.7 V vs. RHE in argon saturated 0.1 M HClO₄ (Figs. 2b and S1). The test condition was intended to mimic the excursion to high potential that a PEMFC cathode experiences during start-up/shut-down or fuel starvation events. These ADTs provide an efficient way to establish the resistance of a material to electrochemical corrosion.

The electrochemical features observed in CV scans during the ADT depended on the polarization potential (Fig. 2b). A broad oxidation peak was typically observed in the potential range of 0.5–0.8 V vs. RHE. This peak was attributed to one-electron transfer on quinone/hydroquinone (Q/HQ) groups by carbon oxidation [29]. A commercial a-CB sample was also tested for comparison. To compare the degree of the surface oxidation, the charge density of the reaction was calculated and normalized by the initial value. The a-CB showed a progressive increase of surface oxide species, almost linearly proportional to the number of potential cycles. As a result, a-CB was highly oxidized by the electrochemical oxidation process during the ADT. For the case of a-CB@pg-CN, however, no apparent variation existed in the Q/HQ potential region after cycling, indicating that no electrochemical oxidation occurred on the samples. Importantly, excellent electrochemical stability of the a-CB@pg-CN samples was observed up to 1.85 V, the position of the valence band level (Fig. 2a); however, from potential cycling conditions higher than 1.9 V, a-CB@pg-CN started to show signs of oxidation (Fig. S2). This result provides strong support for our assessment of electrochemical stability using the electron band energy level for possible electrochemical processes in a given potential range.

3.3. Properties of a-CB@pg-CN as supporting material

The abundant presence of electron lone pairs from nitrogen-rich six-fold interstices between tri-s-triazine units and N–H functional groups at the end sites of pg-CN may serve as stabilizing sites for metal catalyst nanoparticle species, reducing aggregation and potentially enhancing the catalytic activity. We found that platinum (Pt) (20 wt% Pt) was successfully deposited onto an a-CB@pg-CN supporting layer with the same average particle size as on a-CB supports and with a similar particle size distribution. There was no significant increase in Pt particle size at higher loadings (50 wt% Pt) on the a-CB@pg-CN, which indicated that the surface nucleation sites for supports was sufficient to accommodate high loading of nanoparticles; however, it resulted in larger catalyst particle size on the a-CB support at the same condition (Fig. S3).

This is very important, because although graphitized carbon-based nanomaterials feature unique advantages for such designated catalysis supports due to their crystalline molecular structures, this concept has not been explored extensively due to the much fewer nucleation sites. This paucity of nucleation sites is related to carbon surface defects and highlights the importance of metal catalyst–defect bonds. Technically, a post-defect-formed graphitized carbon structure could be decorated with catalyst and exhibit similar catalytic behavior, but such an approach is unattractive for industrial processes.

Major obstacles to the use of pg-CN as an electrocatalyst support for metal nanoparticles are its poor conductivity and the manipulation required to develop high surface area through the use of templates. As

discussed above, these pg-CN materials are two-dimensional (2D) semiconductors with band gaps up to ca. 2.7 eV, which severely limits their intrinsic electrical conductivity and can negatively impact their practical applications. The latest experimental and theoretical research shows that electrical conductivity can be improved when pg-CN materials come into close contact with conductive forms of carbon in a composite or hybrid electrode system [30].

3.4. Coating process and mechanism

Our synthetic strategy was to uniformly coat a-CB with 2D polymeric graphitic nanosheets with nitrogen-enriched surface functionalities ordered on lattice sites, and control the molecular weight of the polymer molecules on the particle surface to allow a uniform and ultrathin coating of particles within the narrow interparticle space. The synthetic strategy to grow 2D nanosheets by a polymerization method into ultrathin shells on nanoscale spherical colloidal templates is a simple but powerful technique. In our approach, the polymerization method was applied directly to a-CB without the use of any additional chemicals or surface pretreatments. More importantly, such synthetic strategy is versatile, and the shell thickness and multiple layers of such core@shell nanostructures can be controlled easily by manipulating the amounts of pg-CN precursors used to prepare the a-CB@pg-CN.

Typically, the as-synthesized a-CB@pg-CN hybrid consisted of a multilayered stacked nanosheet structure of pg-CN on a-CB particles, of which the electron diffraction pattern showed complex Moiré patterns (Fig. S4). Thermogravimetric analysis (TGA) quantified the mass content of the pg-CN coating on a-CB@pg-CN. Significant weight loss occurring between 500 and 600 °C corresponded to thermal decomposition of pg-CN, from which the loading of pg-CN was calculated to be 17, 35, and 49 wt% for the a-CB@pg-CN samples tested in this work (Fig. S5a).

The surface area of the prepared samples was examined using nitrogen adsorption/desorption isotherms (Fig. S6 and Table S1). A comparison of the electrical conductivity measured by impedance measurement was made in this study in Table S2.

We used synchrotron-based near-edge X-ray absorption fine structure (NEXAFS) and X-ray photoelectron spectroscopy (XPS) to further probe the lateral structure of the pg-CN multilayered nanosheets of the composites (Fig. 3). The NEXAFS patterns of pure pg-CN and a-CB@pg-CN are shown in Fig. 3a. All of the identified peaks of the as-synthesized a-CB@pg-CN correspond to those of the pure pg-CN structure: in the nitrogen K-edge NEXAFS spectrum, a-CB@pg-CN (17 wt%) shows two characteristic p resonances at 399.7 and 402.6 eV corresponding to aromatic C–N–C coordination in one tri-s-triazine hetero ring (N1, see the inset of Fig. 3a) and N–3C bridging among three tri-s-triazine moieties (N2, see the inset of Fig. 3a) [31].

However, the N2 resonance was less intense for a-CB@pg-CN than for pg-CN, which was interpreted as a partial breaking of N–3C bridges for pg-CN formed on the a-CBs. Most XPS peaks of a-CB@pg-CN were in good agreement with those of pure pg-CN, but polyheptazines form poorly-organized ribbon-like structures, such as those found in melon, which are terminated laterally by –NH– and –NH₂ groups (Fig. 3b, c and S5b). Based on deconvolution of the N1s XPS spectrum, the relative ratio of N–H in pg-CN of the a-CB@pg-CN was high at 10.4%, which is larger than the 5.2% for pure pg-CN. This may indicate different polymerization degrees of stacked pg-CN on a-CBs. As the precursor amount for pg-CN increased, the degree of polycondensed structures at the surface increased with the disappearance of N–H groups at the edges (Fig. 3b, c, and Fig. S5b). Furthermore, we note that for lower pg-CN loadings, there was a different angular dependence of the characteristic resonances, which suggested that the new species were precursors of pg-CN (Fig. 3a). The final polycondensed a-CB@pg-CN structures, according to the precursor (i.e., dicyandiamide) amount, are schematically shown in Fig. 3d.

The defective species assigned to a-CBs that coordinated to form a-

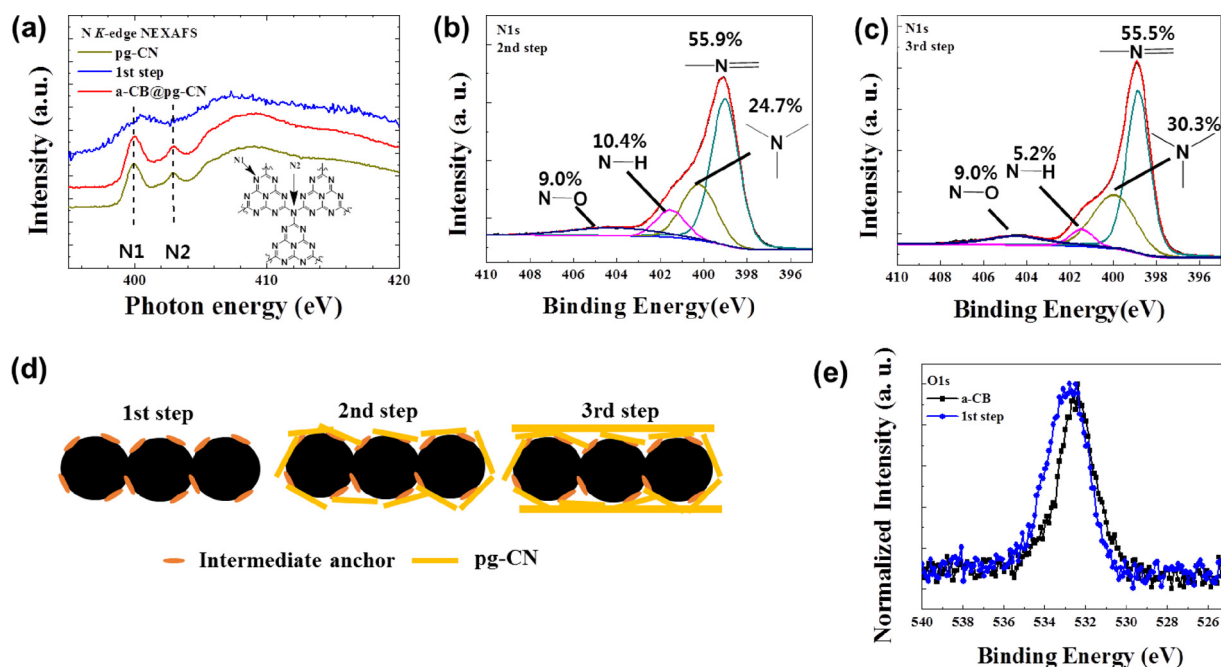


Fig. 3. Structural characterization of a-CB@pg-CN. (a) N K-edge NEXAFS of pg-CN, a-CB@pg-CN in 1st step and a-CB@pg-CN, N1s XPS spectra of a-CB@pg-CN in the (b) 2nd step and (c) 3rd step, (d) schematic illustration of pg-CN's coating profiles on a-CBs, (e) High-resolution O1s XPS of a-CB and a-CB@pg-CN in the 1st step.

CB@pg-CN were likely associated with the breakage of the N–3C bridging bonds at the edge of pg-CN moieties. Correspondingly, the presence of a new O1s XPS peak for a-CB@pg-CN was observed (Fig. 3e), which may indicate a new oxygen bonding species formed during the growth of pg-CN nanodomains on the a-CB surface. These observations suggest the generation of chemical bonds between these two materials during the coupling of pg-CN and a-CB; such chemical bonds do not exist in physical mixtures of pg-CN and a-CB. These interlayer bonds can provide high interconnectivity between parallel layers of pg-CN and a-CB for rapid electron transfer and boosting of the hybrid's electrocatalytic activity.

3.5. Electrochemical stability and performance of Pt/a-CB@pg-CN

3.5.1. Half-cell test

We then turned to rotating disk electrode (RDE) measurements in 0.1 M HClO₄ under an oxygen atmosphere in a half-cell apparatus to evaluate the ORR activity of Pt catalysts supported on a-CB@pg-CN (Figs. 4 and S7). A state-of-the-art commercial Pt/a-CB catalyst (27.7 wt % Pt, Tanaka) was also measured under the same conditions for comparison. The results show that the catalytic activity of the a-CB@pg-CN-based Pt catalyst depended on the amount of coated pg-CN. Among the test samples, the Pt/a-CB@pg-CN (17 wt%) exhibited the optimal catalytic activity of the half-wave potential to 0.9 V and an onset potential of about 1.0 V, comparable to the Pt/a-CB catalyst with the same loading of 0.046 mg Pt cm⁻². The poorer electrochemical activities of high pg-CN loaded samples were due to impediment of transport processes in the electrode by the increased shell thickness.

The enhanced ORR performance and specific activity of optimal Pt/a-CB@pg-CN compared with Pt/a-CB was attributed to a synergistic effect between Pt and electrochemically active functional groups in pg-CN (Fig. S8). As revealed by previous studies [32], these nitrogen groups at the edge of the graphitic layers can favor oxygen adsorption on adjacent carbon atoms, and accelerate the rate-determining first electron-transfer step during the ORR. Quantum theory calculations and previous experimental results also suggest that doping of quaternary nitrogen group into graphene matrices can induce a non-uniform electron distribution and short carbon-nitrogen single bonds,

comparable to oxygen-oxygen single bonds, which would facilitate oxygen adsorption and subsequent disassociation/weakening of oxygen-oxygen double bonds [32]. Also, the tight contact between a-CB and pg-CN favored electron conduction and benefited the ORR.

We further tested the long-term ORR stability of the electrodes using an ADT condition of cycling between 0.6 and 1.2 V at 250 mV s⁻¹ in oxygen-saturated 0.1 M HClO₄ electrolyte. Voltammograms showed that the ADT had significantly less impact on Pt/a-CB@pg-CN than on Pt/a-CB (Fig. 4). The electrochemically active surface area (ECSA) was periodically measured during the ADT (Figs. 4b, d and S9). Clearly, the ECSA retention rate of the Pt/a-CB@pg-CN was much higher than that of a-CB-based ones. Table 1 lists the main characteristics of the normalized ECSAs and the cycling stability of the Pt/a-CB@pg-CN; comparative data for previously reported support materials-based Pt electrodes are also shown. The superior durability of the Pt/a-CB@pg-CN electrode is clearly evident. Importantly, our a-CB@pg-CN-based Pt electrodes exhibited the most stable properties.

3.5.2. Single cell test

We constructed a single unit cell PEMFC device using the a-CB@pg-CN-based Pt electrodes to demonstrate the potential of our catalyst for real fuel cell devices. The Pt/a-CB catalysts were also tested under the same conditions for comparison. An open-circuit voltage of 0.952–0.957 V was measured for Pt/a-CB@pg-CN and Pt/a-CB, consistent with that previously reported for PEMFCs. Current–voltage curves (Fig. 5) clearly revealed that the PEMFC with the Pt/a-CB@pg-CN electrocatalyst displayed similar power densities as Pt/a-CB with the same catalyst loading. Notably, no obvious drop was observed in long-term current–voltage testing of the Pt/a-CB@pg-CN; the air electrode made with it functioned robustly for more than 10,000 cycles without any loss of voltage, highlighting again the structural stability of the a-CB@pg-CN support.

The excellent structural stability of the core@shell-like a-CB@pg-CN support used in the PEMFC electrode was also inferred from transmission electron micrographs of the Pt catalyst particles in the electrode taken after ADT. Fig. 6 shows that no obvious size change was observed, and the morphology of the Pt structure remained highly dispersed after the ADT cycles. This indicated strong catalyst–support

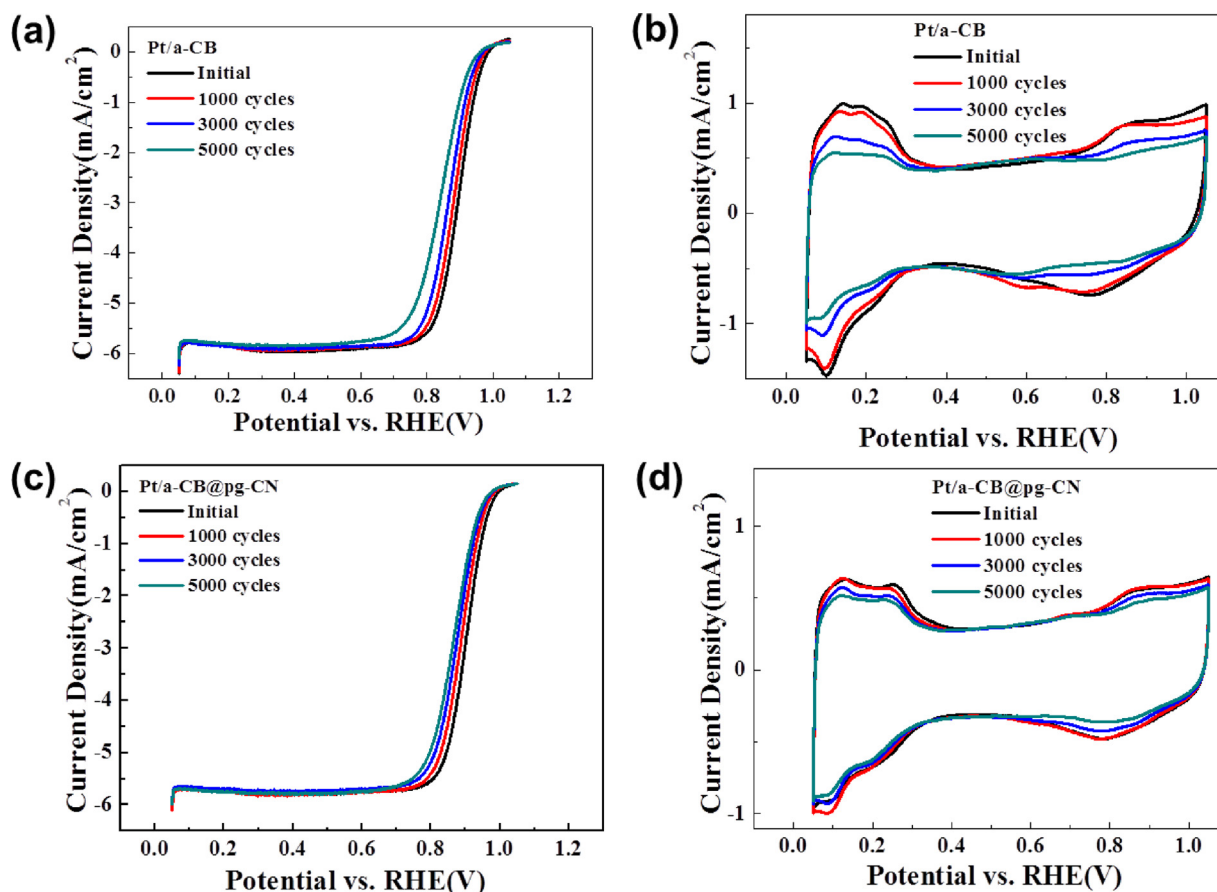


Fig. 4. ORR polarization curves and cyclic voltammograms (CVs) of (a), (b) Pt/a-CB and (c), (d) Pt/a-CB@pg-CN catalysts before and after potential cycling between 0.6 and 1.2 V.

interactions and excellent corrosion stability of the supports during electrochemical cycling.

3.6. DFT calculation

To better understand the enhanced durability of the Pt catalyst supported on a-CB@pg-CN, we performed DFT calculations to establish how the stability of the carbon support and Pt catalyst could be affected by the deposition of a single pg-CN layer on a pure graphite surface (Fig. 7). We first examined the equilibrium potential for surface carbon electrochemical oxidation with water ($C + 2H_2O \rightarrow CO_2 + 4H^+ + 4e^-$) for pure graphite and pg-CN-coated graphite (indicated as a-CB@pg-CN) [39–41]. Table 2 shows that a-CB@pg-CN had

a 0.15 V more positive equilibrium potential for carbon electrochemical oxidation than the a-CB case, which indicated improved resistance of a-CB@pg-CN to carbon corrosion in a fuel cell condition. Note that higher equilibrium potential for carbon oxidation corresponds to higher overpotential. Such enhancement is related to the difference in the cohesive energy (or binding strength) of a carbon atom in a-CB and a-CB@pg-CN. Our DFT calculation predicted a 0.31 eV higher cohesive energy of a carbon atom coordinated to three N atoms in a-CB@pg-CN than a carbon atom coordinated to three C atoms in a-CB. This implies that a-CB@pg-CN is energetically more stable than a-CB and is less likely experience carbon corrosion.

Next, we investigated the binding energy of Pt species (Pt_1 and Pt_{13}) on the surface of a-CB and a-CB@pg-CN. The binding energy is

Table 1

Summary of Pt electrocatalysts on various carbon supports for the electrochemically active surface area (ECSA) retention upon electrochemical potential cycling experiments.

No.	Electrocatalyst name	Durability studies						Reference
		Protocol					ECA retention (%)	
		Potential range (V)	No. of Cycles	Atmosphere	Temperature	Electrolyte		
0	Pt/a-CB@pg-CN	0.6–1.2	5000	O ₂	R.T.	0.1 M HClO ₄	81	This study [33] [20] [34] [21] [35] [36] [37] [38]
1	Pt/meso-BMP	0.5–1.0	10,000	N ₂	R.T.	0.1 M HClO ₄	76	
2	Pt/NRGO	0.6–1.2	4000	–	R.T.	0.5 M H ₂ SO ₄	70.6	
3	Pt/NMC-2	0.25–1.45	750	–	R.T.	0.1 M H ₂ SO ₄	44	
4	Pt/CN _{8,4}	0.6–1.2	4000	O ₂	R.T.	0.5 M H ₂ SO ₄	42.5	
5	Pt/CNC(1000)	0.6–1.24	5000	N ₂	R.T.	0.5 M H ₂ SO ₄	50	
6	Pt/PCNFs	0.6–1.4	1000	N ₂	R.T.	0.5 M H ₂ SO ₄	50	
7	Pt/C@PANI(30%)	0.0–1.2	1500	N ₂	R.T.	0.5 M H ₂ SO ₄	70	
8	Pt/CNTF-1	0–1.24	5000	O ₂	R.T.	0.5 M H ₂ SO ₄	60	

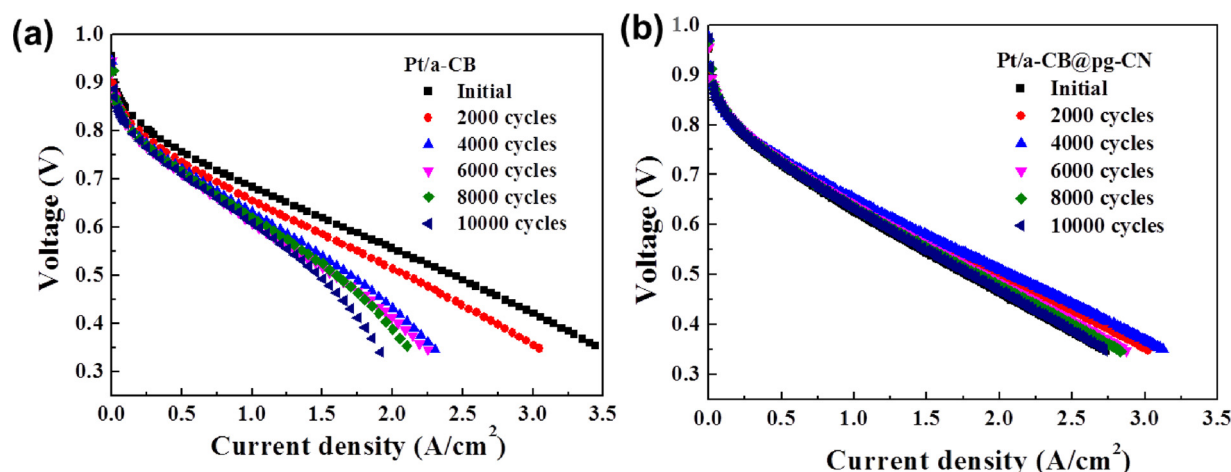


Fig. 5. Polarization curves of PEMFCs using (a) Pt/a-CB and (b) Pt/a-CB@pg-CN cathode electrocatalysts at different number of potential cycles in the ADT.

associated with the durability of Pt particles on the carbon support. That is, a weakened interaction between Pt particles and the carbon support due to decreased binding energy tends to accelerate the dissolution and diffusion of Pt particles in the carbon support, leading to the agglomeration or loss of Pt species [14,39]. Table 2 shows that Pt₁ and Pt₁₃ on a-CB@pg-CN had binding energies that were higher by 1.80 and 2.37 eV, respectively, than the graphite case, indicating enhanced stability of Pt species on a-CB@pg-CN.

With the validation of improved durability of Pt particles supported

on an a-CB@pg-CN system, we also calculated the free energy diagram for the ORR and the total density of states (TDOS) to better understand the ORR activity and electrical conductivity of a-CB@pg-CN. Fig. 7b graphs the variation of the free energy along the ORR pathways on the surface of a-CB and a-CB@pg-CN with Pt₁₃ (denoted as Pt₁₃-a-CB and Pt₁₃-a-CB@pg-CN, respectively) at the onset potential of the ORR. Here, we accepted the simple ORR model from the previous study [42] (which begins with O₂ dissociation before hydrogenation and is sufficiently accurate to provide insight into the activity of different catalyst

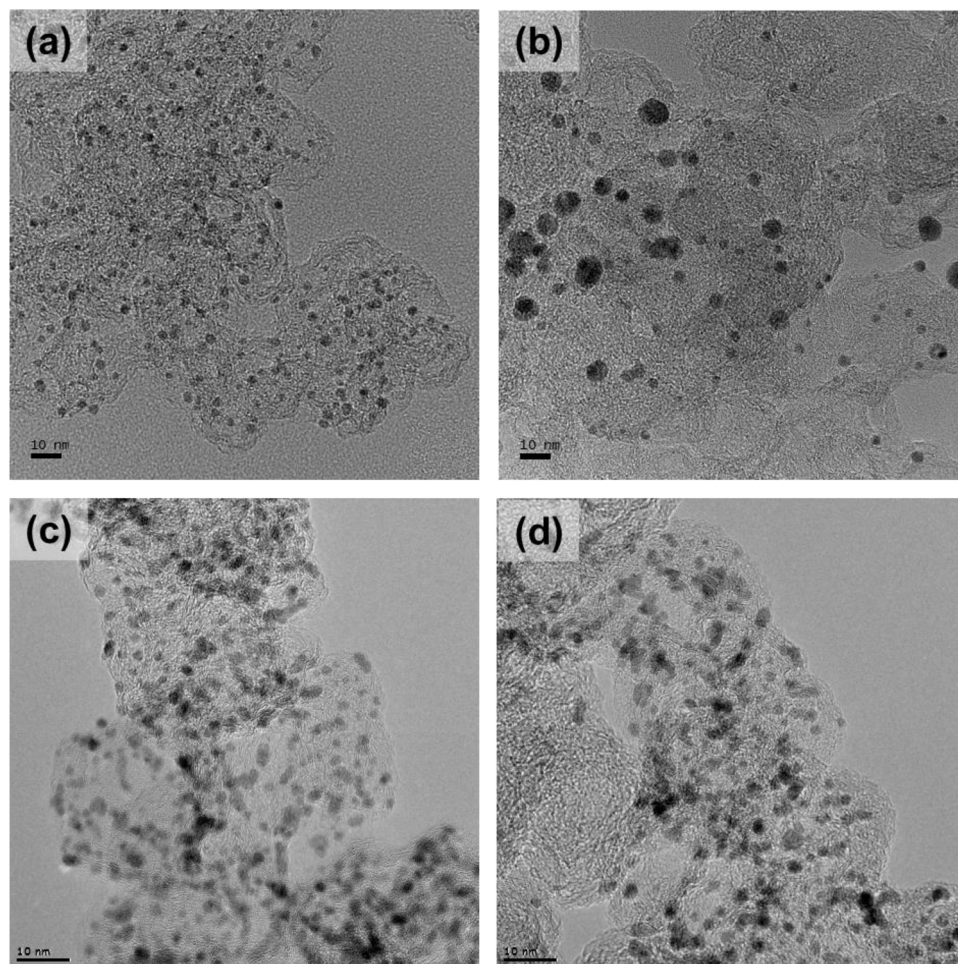


Fig. 6. TEM images of (a), (b) Pt/a-CB and (c), (d) Pt/a-CB@pg-CN measured before and after the ADT, respectively.

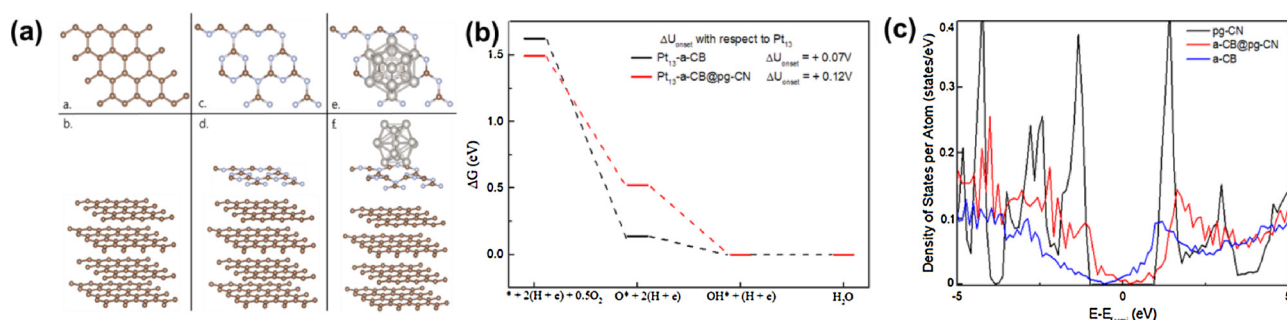


Fig. 7. (a) The surface models of a-CB, a-CB@pg-CN and Pt₁₃-a-CB@pg-CN. The upper figures and lower figures indicate the top and side view of graphite, a-CB@pg-CN and Pt₁₃-a-CB@pg-CN, respectively. Yellow, blue, and gray balls represent the C, N and Pt atom, respectively. (b) Free energy diagram for ORR over Pt₁₃-a-CB (black), and Pt₁₃-a-CB@pg-CN (red). A change in onset potential with respect to Pt₁₃, denoted as ΔU_{onset} , is calculated for Pt₁₃-a-CB and Pt₁₃-a-CB@pg-CN. (c) Total density of states plots of a single atomic pg-CN layer, a-CB@pg-CN, and a-CB, which are represented in black, red and blue line respectively. The dotted line at 0 eV refers to the Fermi level position (For interpretation of the references to colour in this figure legend, the reader is referred to the web version of this article).

Table 2

Calculated equilibrium potential (in V) for the surface carbon electrochemical oxidation ($C + 2H_2O \rightarrow CO_2 + 4H^+ + 4e^-$) and binding energy (in eV) of a single Pt atom (Pt₁) and Pt icosahedral cluster (Pt₁₃) onto a-CB and a-CB@pg-CN.

Equilibrium potential for $C + 2H_2O \rightarrow CO_2 + 4(H^+ + e^-)$	a-CB	a-CB@pg-CN
	0.17	0.32
Binding energy of Pt ₁	−0.48	−2.28
Binding energy of Pt ₁₃	−2.88	−5.25

surfaces toward ORR), although the ORR mechanism remains controversial.

We found that the free energy change of $OH^\bullet + (H^+ + e^-) \rightarrow H_2O$ for both Pt₁₃-a-CB@pg-CN and Pt₁₃-a-CB at the onset potential of ORR was zero, indicating that $OH^\bullet + (H^+ + e^-) \rightarrow H_2O$ was the rate-determining step in the ORR. This is in good agreement with previous results [43,44]. Note that the other reaction steps in the ORR occur more rapidly than $OH^\bullet + (H^+ + e^-) \rightarrow H_2O$ due to the highly negative free energy changes. Additionally, our calculations showed that the onset potentials of the ORR for Pt₁₃-a-CB and Pt₁₃-a-CB@pg-CN with respect to the unsupported Pt₁₃ case (ΔU_{onset}) shifted in the positive direction by 0.07 and 0.12 V, respectively, indicating little change or a slight improvement of ORR activity with the deposition of pg-CN monolayer onto the surface of pure a-CB.

Fig. 7c displays the TDOS for a single atomic pg-CN layer, a-CB@pg-CN, and a-CB systems. The single pg-CN layer case exhibits a bandgap of about 2.0 eV between the top of the valence band and the bottom of the conduction band, whereas no band gap is observed for the a-CB case. This result suggests poor electrical conductivity for the single pg-CN case; increased internal resistance may reduce the operational voltage. On the other hand, our DFT calculations predicted no bandgap for the a-CB@pg-CN system, indicating that the electrical conductivity of a-CB is unchanged by the formation of a pg-CN shell layer.

4. Conclusion

Our study indicates that coupling of 2D pg-CN layered nanosheets with a-CBs in the core@shell configuration resulted in the formation of a simple, robust, and highly electrochemically stable catalyst support, the electrocatalytic ORR performance of which was more stable than that of state-of-the-art a-CB supports for PEMFC devices with simultaneously high energy and power densities. Experimental observations in combination with DFT calculations revealed that its unusual electrocatalytic properties originate from an intrinsic chemical and electronic coupling that synergistically reduces electrochemical corrosion kinetics and promotes catalyst-support interactions. This finding expands our

knowledge of electrochemically stable carbon supports and paves the way for the performance-oriented molecular design of these innovative materials.

Competing financial interests

The authors declare no competing financial interests.

Acknowledgements

This work was supported by the KIST Institutional Programs (2E27301 and KIST Young Fellow). This work was financially supported by the KIST-UNIST partnership program (2V05120/1.160097.01). This work was supported by the Global Frontier R&D Program on Center for Multiscale Energy System funded by the National Research Foundation under the Ministry of Science, ICT & Future Planning, Korea (2016M3A6A7945505). This work was supported by the New and Renewable Energy of the Korea Institute of Energy Technology Evaluation and Planning (KETEP) granted financial resource from the Ministry of Trade, Industry & Energy, Republic of Korea (No. 20153010031920). Moreover, it was partially supported by the National Research Foundation of Korea (NRF) Grant funded by the Ministry of Science, ICT & Future Planning (NRF-2016M1A2A2937136). This research was supported by the Technology Development Program to Solve Climate Changes of the National Research Foundation (NRF) funded by the Ministry of Science, ICT, & Future Planning (NRF-2015 M1A2A2056690).

Appendix A. Supplementary data

Supplementary material related to this article can be found, in the online version, at doi:<https://doi.org/10.1016/j.apcatb.2018.05.081>.

References

- [1] F.T. Wagner, B. Lakshmanan, M.F. Mathias, J. Phys. Chem. Lett. 1 (2010) 2204–2219.
- [2] H.A. Gasteiger, S.S. Kocha, B. Sompalli, F.T. Wagner, Appl. Catal. B: Environ. 56 (2005) 9–35.
- [3] W. Yu, M.D. Porosoff, J.G. Chen, Chem. Rev. 112 (2012) 5780–5817.
- [4] H.A. Gasteiger, N.M. Marković, Science 324 (2009) 48–49.
- [5] X. Zhao, M. Yin, L. Ma, L. Liang, C. Liu, J. Liao, T. Lu, W. Xing, Energy Environ. Sci. 4 (2011) 2736–2753.
- [6] C. Song, J. Zhang, Electrocatalytic oxygen reduction reaction, in: J. Zhang (Ed.), PEM Fuel Cell Electrocatalysts and Catalyst Layers: Fundamentals and Applications, Springer, London, 2008, pp. 89–134.
- [7] J. Speder, A. Zana, I. Spanos, J.J.K. Kirkensgaard, K. Mortensen, M. Hanzlik, M. Arenz, J. Power Sources 261 (2014) 14–22.
- [8] M. Arenz, A. Zana, Nano Energy 29 (2016) 299–313.
- [9] X. Yu, S. Ye, J. Power Sources 172 (2007) 145–154.
- [10] S. Maass, F. Finsterwalder, G. Frank, R. Hartmann, C. Merten, J. Power Sources 176 (2008) 444–451.

- [11] K. Yu, D.J. Groom, X. Wang, Z. Yang, M. Gummalla, S.C. Ball, D.J. Myers, P.J. Ferreira, *Chem. Mater.* 26 (2014) 5540–5548.
- [12] S. Zhang, X.-Z. Yuan, J.N.C. Hin, H. Wang, K.A. Friedrich, M. Schulze, *J. Power Sources* 194 (2009) 588–600.
- [13] J. Dillet, D. Spornjak, A. Lamibrac, G. Maranzana, R. Mukundan, J. Fairweather, S. Didierjean, R.L. Borup, O. Lottin, *J. Power Sources* 250 (2014) 68–79.
- [14] N. Mansor, T.S. Miller, I. Dedigama, A.B. Jorge, J. Jia, V. Brázdová, C. Mattevi, C. Gibbs, D. Hodgson, P.R. Shearing, C.A. Howard, F. Corà, M. Shaffer, D.J.L. Brett, P.F. McMillan, *Electrochim. Acta* 222 (2016) 44–57.
- [15] K.N. Wood, R. O'Hayre, S. Pylypenko, *Energy Environ. Sci.* 7 (2014) 1212–1249.
- [16] R. Borup, J. Meyers, B. Pivovar, Y.S. Kim, R. Mukundan, N. Garland, D. Myers, M. Wilson, F. Garzon, D. Wood, P. Zelenay, K. More, K. Stroh, T. Zawodzinski, J. Boncella, J.E. McGrath, M. Inaba, K. Miyatake, M. Hori, K. Ota, Z. Ogumi, S. Miyata, A. Nishikata, Z. Siroma, Y. Uchimoto, K. Yasuda, K. Kimijima, N. Iwashita, *Chem. Rev.* 107 (2007) 3904–3951.
- [17] Y. Shao, G. Yin, Z. Wang, Y. Gao, *J. Power Sources* 167 (2007) 235–242.
- [18] J.H. Kim, J.Y. Cheon, T.J. Shin, J.Y. Park, S.H. Joo, *Carbon* 101 (2016) 449–457.
- [19] S. Ratso, I. Kruusenberg, U. Joost, R. Saar, K. Tammeveski, *Int. J. Hydrogen Energy* 41 (2016) 22510–22519.
- [20] D. He, Y. Jiang, H. Lv, M. Pan, S. Mu, *Appl. Catal. B: Environ.* 132–133 (2013) 379–388.
- [21] Y. Chen, J. Wang, H. Liu, R. Li, X. Sun, S. Ye, S. Knights, *Electrochem. Commun.* 11 (2009) 2071–2076.
- [22] Z. Li, J. Liu, C. Xia, F. Li, *ACS Catal.* 3 (2013) 2440–2448.
- [23] Y. Zhao, R. Nakamura, K. Kamiya, S. Nakanishi, K. Hashimoto, *Nat. Commun.* 4 (2013) 2390–2396.
- [24] J.P. Perdew, K. Burke, M. Ernzerhof, *Phys. Rev. Lett.* 77 (1996) 3865–3868.
- [25] G. Kresse, J. Furthmüller, *VASP the Guide*, Vienna University of Technology, Vienna, 2001.
- [26] P.E. Blöchl, J. Kästner, C.J. Först, *Electronic structure methods: augmented waves, pseudopotentials and the projector augmented wave method*, *Handbook of Materials Modeling*, Springer, 2005, pp. 93–119.
- [27] Y. Zheng, J. Liu, J. Liang, M. Jaroniec, S.Z. Qiao, *Energy Environ. Sci.* 5 (2012) 6717–6731.
- [28] B. Avasarala, R. Moore, P. Haldar, *Electrochim. Acta* 55 (2010) 4765–4771.
- [29] J. Speder, A. Zana, I. Spanos, J.J.K. Kirkensgaard, K. Mortensen, M. Arenz, *Electrochem. Commun.* 34 (2013) 153–156.
- [30] J. Tian, R. Ning, Q. Liu, A.M. Asiri, A.O. Al-Youbi, X. Sun, *ACS Appl. Mater. Interfaces* 6 (2014) 1011–1017.
- [31] Y. Zheng, Y. Jiao, Y. Zhu, L.H. Li, Y. Han, Y. Chen, A. Du, M. Jaroniec, S.Z. Qiao, *Nat. Commun.* 5 (2014) 3783.
- [32] H.-W. Liang, X. Zhuang, S. Brüller, X. Feng, K. Müllen, *Nat. Commun.* 5 (2014) 4973.
- [33] F. Hasché, T.-P. Feller, M. Oezaslan, J.P. Paraknowitsch, M. Antonietti, P. Strasser, *ChemCatChem* 4 (2012) 479–483.
- [34] L. Perini, C. Durante, M. Favaro, V. Perazzolo, S. Agnoli, O. Schneider, G. Granozzi, A. Gennaro, *ACS Appl. Mater. Interfaces* 7 (2015) 1170–1179.
- [35] X.X. Wang, Z.H. Tan, M. Zeng, J.N. Wang, *Sci. Rep.* 4 (2014) 4437.
- [36] Y. Wang, J. Jin, S. Yang, G. Li, J. Qiao, *Electrochim. Acta* 177 (2015) 181–189.
- [37] S. Chen, Z. Wei, X. Qi, L. Dong, Y.-G. Guo, L. Wan, Z. Shao, L. Li, *J. Am. Chem. Soc.* 134 (2012) 13252–13255.
- [38] X.X. Huang, Y. Chen, X.X. Wang, J.N. Wang, *J. Mater. Chem. A* 3 (2015) 7862–7869.
- [39] H. Tang, Z. Qi, M. Ramani, J.F. Elter, *J. Power Sources* 158 (2006) 1306–1312.
- [40] B.J. Eastwood, P.A. Christensen, R.D. Armstrong, N.R. Bates, *J. Solid State Electrochem.* 3 (1999) 179–186.
- [41] Y. Shao, G. Yin, Y. Gao, *J. Power Sources* 171 (2007) 558–566.
- [42] J.K. Nørskov, J. Rossmeisl, A. Logadottir, L. Lindqvist, J.R. Kitchin, T. Bligaard, H. Jonsson, *J. Phys. Chem. B* 108 (2004) 17886–17892.
- [43] J. Greeley, I.E.L. Stephens, A.S. Bondarenko, T.P. Johansson, H.A. Hansen, T.F. Jaramillo, J. Rossmeisl, I. Chorkendorff, J.K. Nørskov, *Nat. Chem.* 1 (2009) 552.
- [44] H.C. Ham, D. Manogaran, K.H. Lee, K. Kwon, S. Jin, D.J. You, C. Pak, G.S. Hwang, *J. Chem. Phys.* 139 (2013) 201104.